JOURNAL OF SPACECRAFT AND ROCKETS
Vol. 46, No. 1, January–February 2009

Entry Trajectory and Aeroheating Environment Definition for Capsule-Shaped Vehicles

Jeffrey S. Robinson* and Kathryn E. Wurster†
NASA Langley Research Center, Hampton, Virginia 23691
and
Janelle C. Mills‡
ViGYAN, Inc., Hampton, Virginia 23666

DOI: 10.2514/1.30998

The Crew Exploration Vehicle presently being developed to return humans from lunar missions will typically experience entry environments far more severe than those for return from low-Earth orbit. Certification of the thermal protection system materials for these environments, and ultimately for Mars return, will require extensive testing. As part of an effort to bound the required testing capability, trajectories and the associated aeroheating environments were generated for more than 60 unique entry cases. Using the Apollo Command Module as the baseline entry system, trajectories for a range of lunar and Mars return Earth-entry scenarios were developed using a 3-degree of freedom trajectory simulation. For direct entry, a matrix of cases that reflects expected minimum and maximum values of vehicle ballistic coefficient, inertial velocity, and flight-path angle at entry interface was considered. For aerocapture, a range of values of initial velocity and ballistic coefficient was examined that, when combined with appropriate initial flight-path angles, enable the vehicle to achieve low-Earth orbit by employing either a full-lift-vector-up or full-lift-vector-down attitude. For each trajectory, aeroheating environments, intended to bound the thermal protection material system requirements for likely concepts, were generated using engineering methods. The trades examined in this study distinguished the classes of missions/concepts that will require ablative systems as well as those for which reusable systems may be feasible. Results highlight those entry conditions and modes suitable for human flight, considering vehicle deceleration levels experienced during entry. The aeroheating environments generated in this study can be used by the vehicle designer to assess the material testing limits and facility requirements for a broad range of concepts and missions.

Nomenclature

C_D	=	drag coefficient
C_L	=	lift coefficient
D	=	diameter, m
g	=	Earth gravitational acceleration
L/D	=	lift-to-drag ratio
R	=	nose radius, m
R_{eff}	=	effective radius, m
Xc	=	axial coordinate, m (Apollo Command Module)
Zc	=	symmetry plane coordinate, m (Apollo Command Module)
ε	=	emissivity

I. Introduction

IN RESPONSE to the President's 2004 announcement of the Vision for Space Exploration (VSE) [1], NASA initiated an effort to develop and evaluate various thermal protection systems (TPS) and high-temperature material concepts for potential use on the Crew Exploration Vehicle (CEV). As outlined in the VSE, the CEV will one day carry astronauts back to the moon and eventually beyond, and return them to Earth. In support of this activity, trajectories and associated aerothermal environments for several Earth-entry scenarios were generated. The analyses performed, including the assumptions, methods, and general approach used to generate the Earth-entry environments, as well as a sampling of the results, are described.

A key focus of this multicenter NASA effort was to establish the materials testing environments likely to be required to enable flight certification of the required TPS for human spaceflight. The process of "man" rating a vehicle, including its material systems, is an enormous challenge and an early assessment of vehicle environments is required to bring the necessary testing capability on line in a timely fashion. Determination of an expected range of environments will allow NASA to assess the need for facility upgrades and/or development to enable the VSE as established by the President. Although the Apollo experience provides some insight into the expected environments for lunar return, the anticipated scale increase and the extension to Mars return velocities are anticipated to extend the envelope of environments testing that will be required. This study was undertaken as a first step in the process to define that envelope.

Missions considered at the outset of the study included both manned and robotic missions, to and from low-Earth orbit (LEO), geosynchronous orbit, the moon and Mars, as well as extended planetary missions. The approach to mission selection takes into consideration two key issues: first, since the decision to retire the shuttle had already been made, what would be the most likely next step for NASA's exploration programs, and second, what would the most significant challenges be in terms of human-rating materials/concepts to support these missions? The necessity to human rate the materials and concepts in itself represents one of the greatest challenges. Although the robotic missions generally must withstand much more severe space environments, particularly in terms of extended trip duration and ionizing radiation, the consequence of failure for an unmanned mission is deemed much less damaging to

Presented as Paper 7949 at the 14th AIAA/AHI International Space Planes and Hypersonic Systems and Technologies Conference, Canberra, Australia, 6–9 November 2006; received 13 March 2007; revision received 30 May 2008; accepted for publication 2 June 2008.

*Aerospace Engineer, Vehicle Analysis Branch, Mail Stop 451. Senior Member AIAA.
†Senior Research Engineer, Vehicle Analysis Branch, Mail Stop 451. Associate Fellow AIAA.
‡Computer Scientist, Mail Stop 451.

the future of exploration. The decision was therefore made in this study to focus on the atmospheric entry environments and to concentrate primarily on manned mission requirements.

II. Methodology

At the time this work was performed, little definition existed for the VSE and its associated space exploration architecture. Various exploration architecture studies were under way and were reviewed, as were the industry proposed concepts for the CEV. For this work, the Apollo Command Module [2], shown in Fig. 1, was selected as the baseline entry system because of its apparent relevance to several CEV concepts under consideration at the time, together with the availability of an extensive database. To adequately cover the potential design space, this study examined a range of direct and aerocapture Earth reentry trajectories from lunar and Mars return conditions, as well as entries from LEO. Potential alternate concepts/architectures were represented by a matrix of off-nominal trajectory profiles generated for an expected range of entry velocities, flight-path angles, and vehicle ballistic coefficients that defined the likely mission trade space.

A. Trajectory Analysis

Trajectory analysis was performed using the Program to Optimize Simulated Trajectories II (POST2) code [3], an industry standard trajectory simulation code with over 30 years of development, use, and extensive validation [4–6]. Each trajectory was run with 3 degrees of freedom in translation using the 1976 Standard Atmosphere [7] (no winds) with a rotating, oblate Earth gravity model. The vehicle was commanded to follow the trimmed angle-of-attack profile shown in Table 1. Output data were captured starting at entry interface (EI), 121,920 m (400,000 ft), assumed to define the beginning of the sensible atmosphere and the start of the heating phase of the entry. Landing location (latitude and longitude) and its implication to cross-range requirements was not considered during this study.

For the direct entries, one nominal case, as well as a matrix of off-nominal cases, was generated for lunar and for Mars return conditions, respectively. These matrices of cases reflect reasonably expected minimum and maximum values of vehicle ballistic coefficient (defined as vehicle mass divided by the product of drag coefficient and aerodynamic reference area), inertial velocity, and inertial flight-path angle at EI. For the aerocapture cases, three velocities and three ballistic coefficients (expected high, nominal, and low values) were used along with initial flight-path angles that enabled the vehicle to achieve a low-Earth orbit by employing a full-lift-vector-up or full-lift-vector-down attitude. For reference, the aerodynamic characteristics [8] of the Apollo Command Module are shown in Table 1. The aerodynamic reference area is 12.017 m^2, based upon the diameter of the heat shield. The nominal mass for the command module used in the trajectory simulations was 5500 kg. As a point of comparison, the nominal CEV is approximately 30% larger in scale, with a commensurate increase in mass. Nominal ballistic coefficient for the CEV ranges from approximately 310 to 390 kg/m^2, depending upon the assumed trim angle of attack and vehicle mass, which falls well within the range of ballistic coefficients considered in this study (49 to 488 kg/m^2).

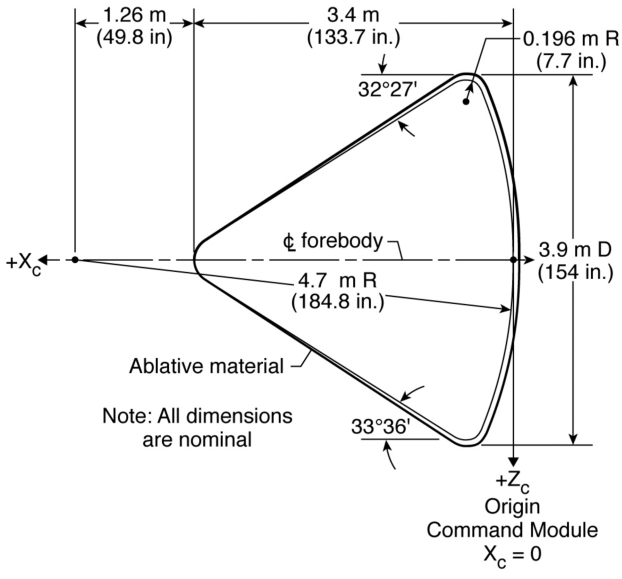

Fig. 1 Apollo Command Module geometry.

The flight-path angle and velocity for the nominal lunar return (case 0) were determined from Apollo lunar mission data [9]. The ballistic coefficient for case 0, 356 kg/m^2, lies in the midrange of that expected for the CEV at entry and as such offers a reasonable representation for a nominal CEV lunar return flight profile. The range of initial off-nominal velocities was selected based upon experience and previous work (examination of actual Apollo entry trajectories and recent lunar abort analyses). Similar information was used to determine the nominal and off-nominal velocities for the Mars return cases. Ballistic coefficients were selected to cover a range of potential entry concepts, including capsules and aerodynamic decelerators, and were achieved by altering the vehicle mass, while maintaining a constant reference area (and therefore the aerodynamics). For the direct entry cases (both lunar and Mars return), the minimum and maximum allowable flight-path angles were determined for each combination of velocity and ballistic coefficient under the constraints of a maximum total acceleration of $10g$ (per Constellation Program systems requirements [10]) and a maximum skip-out altitude of 121,920 m. The only exception was for cases 7 and 8 for the direct return from Mars, where the acceleration limit was relaxed to $12g$ to allow some spread between the minimum and maximum flight-path angles. POST2 was allowed to modulate the bank angle, thereby redirecting the lift vector, to help optimize each case. For the aerocapture cases, the flight-path angle for each combination of velocity and ballistic coefficient was determined by flying the vehicle either full lift vector up or full lift vector down and targeting a 500 km apogee.

B. Aeroheating Environments

1. Nondimensional Distributions

Aeroheating environments were defined for all trajectory cases and were intended to envelope the TPS thermal requirements for likely CEV concepts. These environments were generated for two critical stations on the forebody heat shield, the stagnation region and the "hot" corner, that is, the corner of the heat shield facing into the flow when the vehicle is at an angle of attack. Figure 2 illustrates a representative Apollo Command Module nondimensional heating (convective) and pressure distribution along the symmetry plane, highlighting the stagnation point (corresponding to the point of maximum pressure) and the hot corner locations. The corresponding radiative distribution, not shown here, tends to follow the trend of the pressure distribution with the maximum value occurring in the stagnation region. Recent studies [11] for the CEV show the relative insensitivity of the distributions, when nondimensionalized by an appropriate reference parameter, to both velocity and altitude (density) over the velocity range from approximately 5 to 9 km/s and an altitude range of approximately 45 to 65 km. The same studies show that the distributions are more clearly dependent upon the angle of attack. For the Apollo flight profile, Table 1, and the trajectories generated here, the angle of attack remains relatively constant, ~160–157 deg (equivalent to ~20–23 deg in the aero/aerothermodynamic coordinate system which will be used for the remainder of the paper), throughout the high heating portion of the flight profiles. Thus the hot corner and the stagnation point locations remain relatively fixed over the critical portion of the entry profile and nondimensional distributions such as that illustrated in Fig. 2 can be used in conjunction with engineering reference heating predictions to evaluate the transient heating environments.

Table 1 Apollo Command Module entry profile definition

Mach no.	Angle of attack, deg	C_L	C_D	L/D	Ballistic coefficient, kg/m^2
0.4	167.14	0.24465	0.85300	0.28682	537.39
0.7	164.38	0.26325	0.98542	0.26714	465.16
0.9	161.70	0.32074	1.10652	0.30110	414.26
1.1	154.87	0.49373	1.16970	0.42208	391.86
1.2	155.13	0.47853	1.15600	0.41395	396.50
1.35	154.01	0.56282	1.27880	0.44013	358.44
1.65	153.22	0.55002	1.26570	0.43455	362.14
2.0	153.14	0.53247	1.27210	0.41858	360.34
2.4	153.62	0.50740	1.24120	0.40881	369.32
3.0	154.14	0.47883	1.21670	0.39353	376.74
4.0	156.12	0.44147	1.21480	0.36340	377.32
10.0	156.79	0.42856	1.22460	0.34996	374.30
$\geq$ 29.5	160.06	0.38773	1.28910	0.30076	355.61

2. Engineering Heat-Transfer Prediction Methods

Transient environments for the hot corner and stagnation locations were generated for each trajectory. Relevant aeroheating data, which have been benchmarked where possible to flight, wind-tunnel, and/or detailed computational solutions, were integrated using the aeroheating code MINIVER [12]. MINIVER is an engineering level aerothermal analysis tool with a long usage history and broad user base within the launch vehicle community [13–15]. The MINIVER code provides convenient user access to a number of well-established engineering methods, the most common of which have been heavily validated [12,14,16,17] against flight, wind-tunnel, and detailed computational solutions. Established engineering techniques were used to predict both the convective and radiative components of the incident heating environments at the stagnation point. Fay and Riddell [18], the technique employed in this study to predict the convective heating, is a widely accepted stagnation point heating method that has been in use for nearly 50 years, having been validated against detailed analytical methods and limited flight data. The radiative prediction correlation used for the stagnation region is commonly referred to as Tauber–Sutton [19] and was implemented in MINIVER explicitly for the purposes of this study. This capability is not available in the standard MINIVER release. The Tauber–Sutton correlations are derived from an extensive set of detailed inviscid radiative computational solutions [20] originally generated by Sutton and Hartung. These computational solutions have been previously validated [21] for Apollo-like configurations. The correlation provides an engineering prediction for equilibrium radiative heating over a range of radii from 0.05 to 10 m, velocities from 8 to 18 km/s, and altitudes from 30 to 84 km.

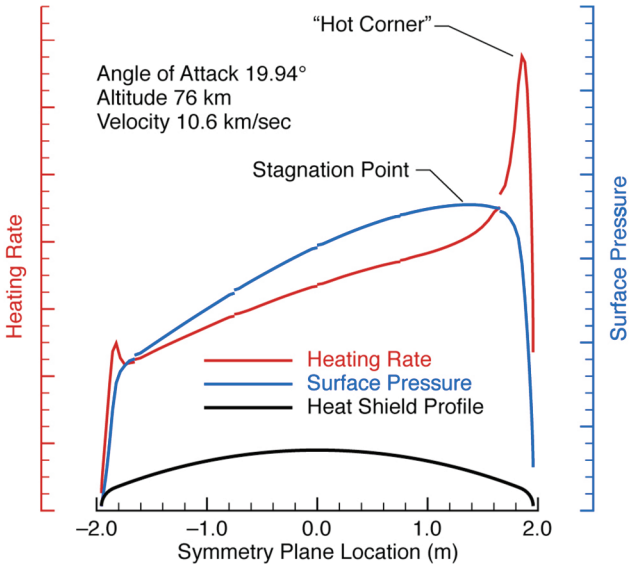

Fig. 2 Apollo forebody heat shield symmetry plane heating and pressure profile at angle of attack.

For a known geometry and condition, both the convective and radiative methods used here are generally quoted to be accurate to within about 20%. Error bars have not been included here for the predicted environments because this is intended only as a broad trade study and not to provide detailed flight environments. The study assumed a simple generalized "Apollo-like" body, equilibrium flowfield conditions, and nonspecific surface materials, and used flight profiles based on a simple point mass with prescribed ballistic coefficients and initial state conditions. It was not intended to provide detailed heating environments for a specific geometry or mission profile, and as such error bars were not considered appropriate for presentation.

3. Effective Nose Radius Approach for Transient Environment Predictions

The engineering solutions used an effective nose radius approach for both the convective and the radiative heating components. The effective radius is selected to match the velocity gradient (convective) and the shock-standoff distance (radiative) for the Apollo configuration at the same condition. The convective radius was determined based on the Apollo Command Module geometry together with data from Zoby and Sullivan [22], originally derived for the zero-degree angle-of-attack case. An effective radius of 4 m (13.1 ft) was used for the calculation of the convective heating at the stagnation point. An angle of attack of ~20 deg would be expected to decrease the effective radius relative to the zero-degree angle-of-attack value, suggesting that the convective results presented here are somewhat nonconservative. Further analysis of the angle-of-attack correction to the radius indicates that a reduction in the effective radius to approximately 2.9 m (9.5 ft) would be appropriate. This correction would increase the convective heating rates shown here by about 15%. For the radiative component the effective radius was determined from Ried [23], based on early Apollo studies. Figure 3 (from [23]) illustrates the Apollo radiative effective radius as a function of angle of attack. For the nominal angle of attack, 20 deg, an effective radius of 3.42 m (11.2 ft) was selected for the radiative heating calculations. Based on the effective radii chosen, the transient environments at the stagnation point were then computed using the relevant trajectory profile and associated freestream conditions. The transient heating at the hot corner was determined

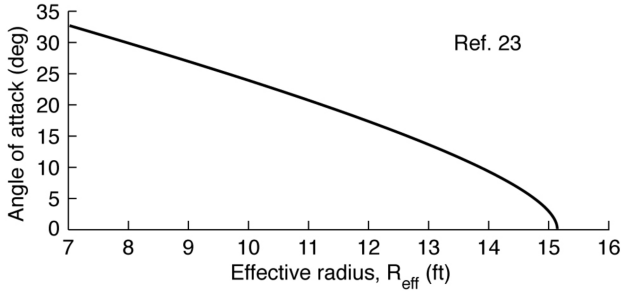

Fig. 3 Effective radius for radiative heating as a function of angle of attack (Fig. 4 from [23]).

relative to the computed stagnation values by using available heating distributions for Apollo, or Apollo-like concepts, similar to that illustrated in Fig. 2. For the case shown, at 19.94 deg angle of attack, the convective rate at the hot corner is observed to be approximately 1.6 times that at the stagnation point. Thus the initial hot corner rate prediction is assumed to be 1.6 times that predicted at the stagnation point throughout the profile. However, because the heating rate is influenced by the wall temperature, it was necessary to perform a hot wall correction for the convective heating. The effective factor is thus reduced somewhat, particularly over the portions of the trajectory profile where the radiative component represents a significant portion of the total heating.

4. Limitations, Assumptions, and General Observations

Radiative heating effects were presumed to be negligible below approximately 9 km/s based on the work of Sutton and Hartung [20] and Sutton [21]. The relative levels of radiative heating and convective heating are strongly dependent upon the flight profile. While the radiative component increases with both velocity and vehicle size, convective heating increases with velocity, but generally decreases with increased vehicle size. These effects are illustrated in Figs. 4 and 5 for nominal lunar and Mars return conditions. The flight profile in turn is strongly influenced by the vehicle's ballistic coefficient, initial flight-path angle, and entry velocity. It should be noted that the convective heating methodology, Fay and Riddell, will likely not be applicable at the higher entry velocities associated with Mars return conditions. Hoshizaki [24] has shown that Fay and Riddell can reasonably predict stagnation heating to velocities up to about 11 km/s (lunar return) if used in conjunction with a viscosity relationship based on nonionized gas. A Sutton and Graves correlation [25] for air might prove a more suitable method for use at these higher velocities. However, for Mars return the radiative contribution tends to dominate the total heating at both aerocapture and direct return conditions, and errors in the convective heating would not be expected to have a significant effect on the total heating rate or load. The entry velocities for lunar return and return from Earth orbit are well within the range of applicability of the convective approach used. Thus, this limitation should not influence the conclusions that can be drawn from these data with respect to the applicability of potential material concepts.

All aeroheating environments were generated using the 1976 Standard Atmosphere model. Both convective and radiative heating were assumed to be dominated by equilibrium flow. In the vicinity of the shock, the flow is not in thermal or chemical equilibrium. Depending upon the speed of the reactions compared to the time it takes for the flow to move from the shock to the body, the flow may not be in equilibrium at the surface (i.e., the nonequilibrium relaxation length may exceed the shock-standoff distance). The relatively small nose radius of the Apollo shape considered here increases the likelihood that nonequilibrium effects would play an important role, at least for the aerocapture cases at the higher altitudes. However, for Apollo 4, predictions from [23] show the nonequilibrium portion of the radiative heating to be relatively insignificant for the entry profile flown. Although the larger scale of the CEV suggests that nonequilibrium effects will not dominate, these effects are presently the subject of study [26,27] within the CEV radiation community. Nonequilibrium effects were considered beyond the scope of this trade study, which was primarily intended to provide direction regarding TPS material testing requirements. Because the present calculations assume equilibrium, the effect of surface catalycity is not considered. In a nonequilibrium flow regime, a catalytic surface would tend to reduce the convective heating levels. For the present cases in which reusable materials can be considered, a noncatalytic coating would be assumed. In the case of an ablating surface, the complexity of the flow and all the chemical reactions precluded the explicit consideration of catalycity in this study.

Turbulent heating effects were not considered in this study. The extremely high laminar heating levels occurring early in the entries at higher altitudes and velocities are expected to exceed the turbulent levels which are likely to occur after the peak heating condition for nonablating surfaces. For an Apollo-like configuration at angle of attack, turbulence is expected to occur first over the "leeward" side of the front face of the heat shield, near the "cooler" corner. The likelihood of transition, particularly during the high heating phase of the entry, is reduced due to the short running lengths associated with the small Apollo Command Module. This study assumed that the laminar heating levels at the hot corner would exceed the turbulent levels at the cooler corner. Thus a TPS designed for the laminar hot corner was assumed to be sufficient. Unknown, however, is the impact of ablation on transition to turbulent flow and this issue was not considered in this limited trade study.

Low-density (i.e., viscous) effects also are not included in the present calculations of the aeroheating environments. A limited assessment using the low-density correlations [17] available in MINIVER for the convective results, performed as part of this effort, showed less then a 2% impact on the total integrated heat load. Nonequilibrium radiation in the low-density regime, which may be more important for smaller vehicles, was not considered in this trade study.

Where convective heating rates are given, they are based on a wall temperature (wall enthalpy) equivalent to a radiation equilibrium value at a constant emissivity of 0.8. The heating rates are presented as radiative, convective, and "total" values. The convective and radiative are "loosely" coupled, in that the radiative heating is allowed to contribute to the increase in wall temperature, thus decreasing the forcing function for the convective heating (enthalpy difference between the recovery and wall values). The total heating rate was assumed to be the simple sum of the convective and radiative contributions. No attempt was made to account for the likely reduction in heating due to coupling between radiation and convection, nor were coupled ablation and blowing flowfield effects

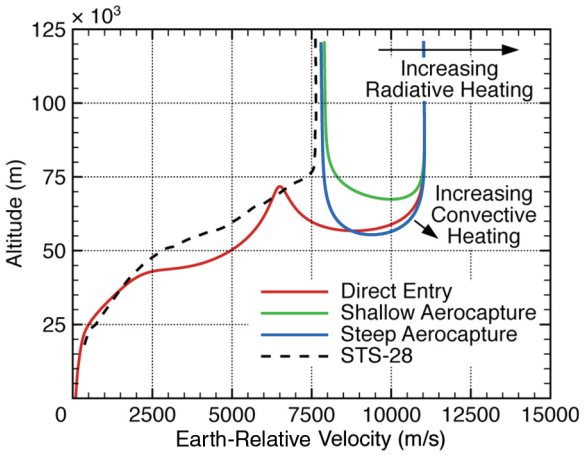

Fig. 4 Typical lunar return trajectories showing areas of increased convective and radiative heating.

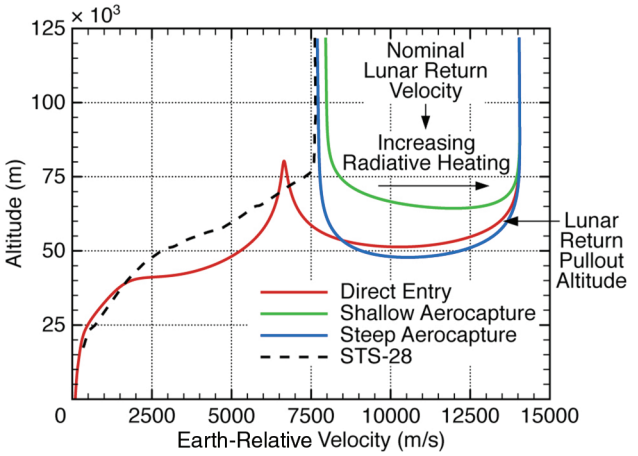

Fig. 5 Typical Mars return trajectories showing areas of increased convective and radiative heating.

considered. The true effect of such a coupling is presently an active area of research [28] in the CEV TPS community. Although ablation may tend to promote transition, the cumulative effects of coupling and blowing are expected to reduce the heating levels compared to the simple summation of the convective and radiative heating used in this study. In calculating the heat-transfer rates, the wall temperature was set to the value of the radiation equilibrium temperature at the previous time step. Small calculation intervals were selected so that it was not necessary to iterate at each time step. Cold wall heating rates and loads were also calculated as these are often the metrics used to determine high-temperature facility requirements for materials testing. For the very high-enthalpy flow conditions at lunar and Mars return conditions (low wall to total enthalpy ratio), the total heat rate (convective) approaches the cold wall value. Aeroheating environments were generated only for the portions of the profile below 121,920 m. Aeroheating effects were assumed to be negligible above this altitude, where free-molecular flow dominates. Heating levels are presented for specific entry cases in the form of heating rates. However, the broad trades are shown as radiation equilibrium temperatures. Although the heating rate is generally the preferred figure of merit, TPS material system capabilities are typically represented in terms of maximum use temperature capability. Thus, radiation equilibrium temperatures in excess of ~2000 K (roughly the maximum reuse temperature for advanced carbon composites) represent conditions for which the radiation equilibrium temperature is not meaningful, but rather suggests that the use of ablative materials is required.

III. Direct Earth Entry at Lunar Return Conditions

Initial conditions for the nominal and off-nominal cases are listed in Table 2 for direct Earth entry at lunar return conditions. Plots of altitude and acceleration as functions of Earth-relative velocity are shown in Figs. 6 and 7, respectively. Of note is the wide variation in acceleration time histories that result from the combination of the initial conditions, ballistic coefficient, and bank angle modulation. Obviously, human-rated missions would not be subjected to such loads; however, our intent here was to explore the potential reasonable trade space for manned and unmanned flights from a TPS perspective. For manned missions, while short durations of higher g levels are tolerated [10], sustained accelerations below $3g$ are typically desired.

Figures 8 and 9 illustrate the relative levels of heating at the stagnation and hot corner locations, respectively, for the nominal case. Note that the heating levels for these two regions are quite similar. Also of note is the relatively "brief" radiative heating pulse. At the point where the radiative heating goes to zero, the total and convective heating are seen to merge. Figures 10 and 11 show the radiation equilibrium temperature and integrated heat load, respectively, for all 13 lunar direct return trajectories. The radiation equilibrium temperature is included on these figures as a rough indicator of the expected wall temperatures, assuming a nonablative,

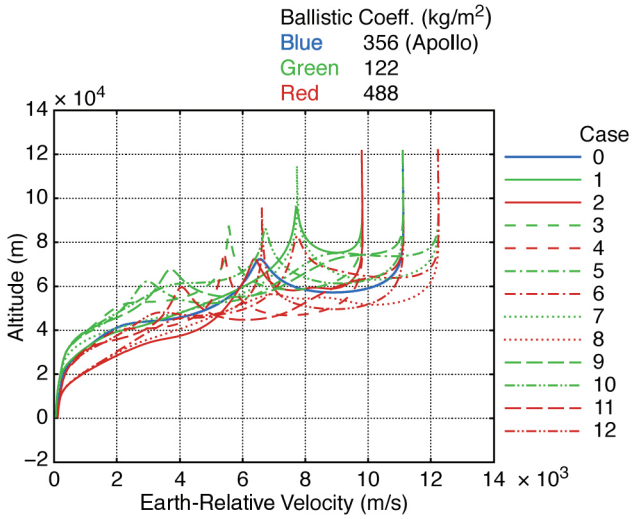

Fig. 6 Geodetic altitude as a function of Earth-relative velocity for all lunar direct Earth return cases.

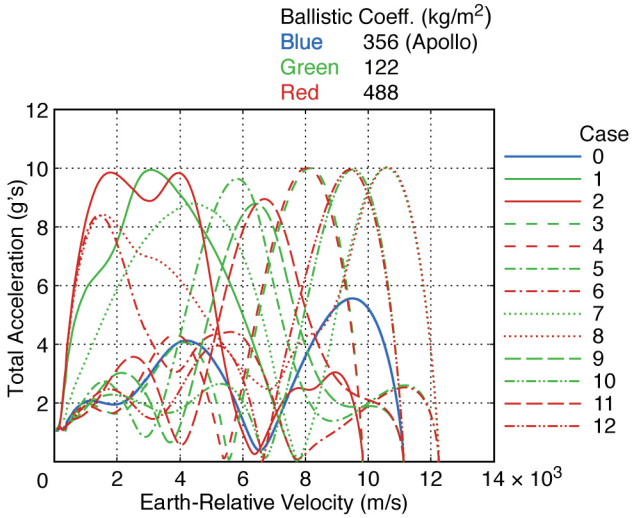

Fig. 7 Total sensed acceleration as a function of Earth-relative velocity for all lunar direct Earth return cases.

insulative TPS. Considering roughly 2000 K as a representative maximum use temperature capability for a reusable ceramic-matrix-composite (CMC) TPS, only the lowest velocity and lowest ballistic coefficient cases appear to be feasible for this type of system. The remaining cases would require the use of ablative systems. As a point of reference, reusable systems in use today on the Shuttle Orbiter

Table 2 Trade matrix for lunar direct return

Case no.	Initial velocity, m/s	Initial flight-path angle, deg	Ballistic coefficient (~Mach 30), kg/m^2
0	11,075	−5.80	356
1	9,765	−3.99	122
2	9,765	−5.21	488
3	9,765	−6.65	122
4	9,765	−7.11	488
5	12,201	−5.09	122
6	12,201	−5.61	488
7	12,201	−6.63	122
8	12,201	−7.40	488
9	11,075	−4.63	122
10	11,074	−6.73	122
11	11,075	−5.13	488
12	11,075	−7.29	488

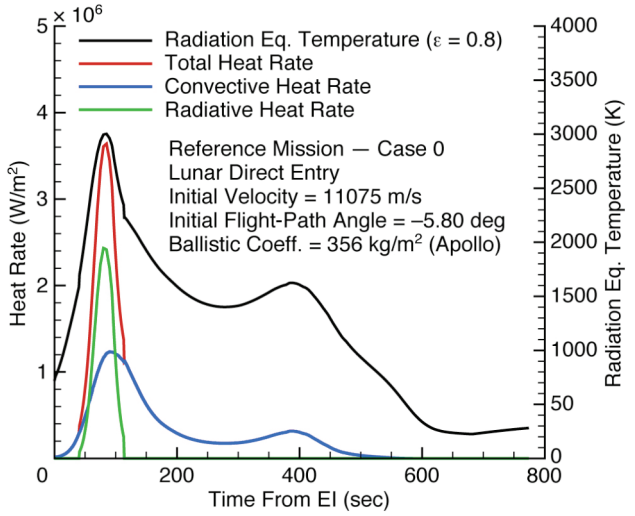

Fig. 8 Stagnation region heating profiles for the nominal lunar direct Earth return case.

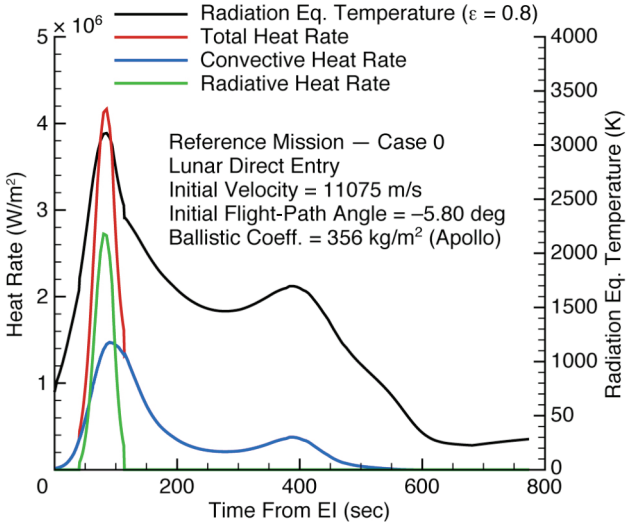

Fig. 9 Hot corner heating profiles for the nominal lunar direct Earth return case.

have maximum use temperatures on the order of 1700 K (2600°F) for the tile systems and 1925 K (3000°F) for the reinforced carbon–carbon leading edges. The integrated heat load (Fig. 11) provides a rough measure of the TPS mass required, with the mass increasing

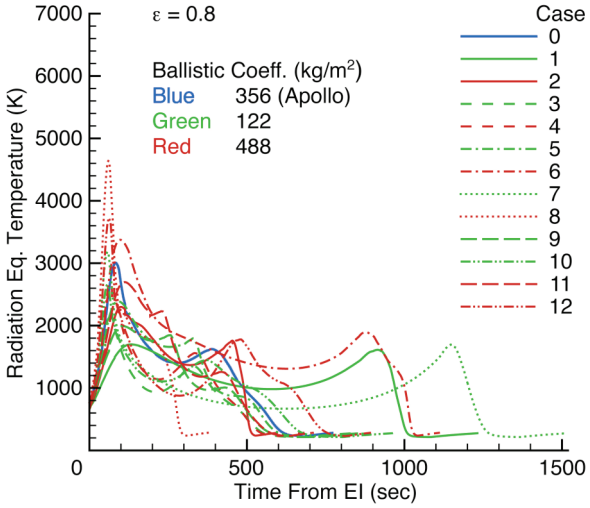

Fig. 10 Stagnation region radiation equilibrium temperature for all lunar direct Earth return cases.

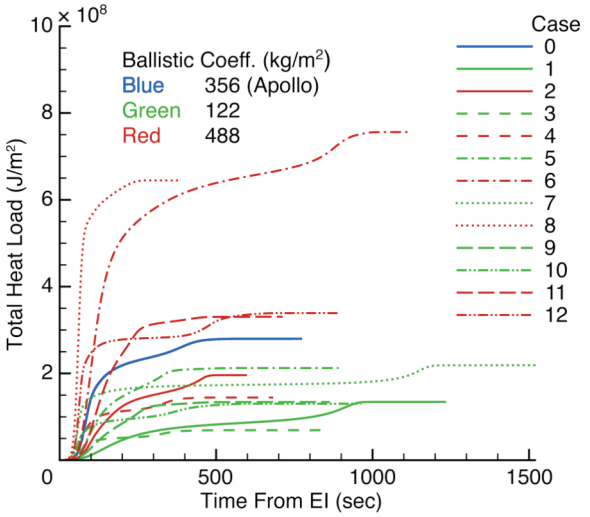

Fig. 11 Stagnation region integrated heat load for all lunar direct Earth return cases.

with increased load. It is readily apparent from the data in these figures that a wide variation in heating rate, integrated heat load, and wall temperature can be expected depending on the vehicle and entry trajectory characteristics.

IV. Direct Earth Entry at Mars Return Conditions

Initial conditions for the nominal and off-nominal cases for the direct Earth entry from Mars return conditions are listed in Table 3. As before, ballistic coefficients were selected to cover a range of potential entry concepts. The original trade matrix consisted of eight cases. Two additional cases at the nominal velocity were added with lower ballistic coefficients (122 kg/m^2 and 49 kg/m^2) so that environments representative of those for an aerodynamic decelerator could be generated. A trailing ballute, deployed at high altitudes to provide the initial deceleration from the extremely high return velocities, would be an example of the type of system to which the low ballistic coefficient cases might apply.

Plots of altitude and acceleration as functions of Earth-relative velocity are shown in Figs. 12 and 13, respectively. Note the change in the velocity scale relative to that in Figs. 6 and 7 for lunar return conditions. Because the kinetic energy is a function of the square of the velocity, it is clear that the high-energy returns from Mars will result in significantly more severe entry environments than those for lunar returns. This is clear in Figs. 14 and 15 which show the relative levels of heating at the stagnation and hot corner locations for the nominal case. Although the total heating levels for these two regions are similar, just as they were in Figs. 8 and 9 for lunar return, the heating levels for Mars return conditions are nearly an order of magnitude higher. Unlike the lunar return where the convective and radiative components are of the same order, for the Mars return conditions the total heat rate is clearly dominated by the radiative component. Figures 16 and 17 show the radiation equilibrium temperature and total integrated heat load, respectively, for all 11 Mars direct return trajectories. Again, significant increases in both quantities are evident when compared to data from the lunar direct return cases. Temperatures are well above the capability of reusable CMCs. In fact, the ballistic coefficients necessary to achieve an acceptable ablator heating rate level, assumed to be on the order of 5–10 MW/m^2, would likely require some type of additional aerodynamic or propulsive deceleration device.

V. Earth Aerocapture from Lunar Return Conditions

The low, medium, and high values of initial velocity and ballistic coefficient used for the Earth aerocapture from lunar return conditions are the same as those selected for the direct lunar entry

Table 3 Trade matrix for Mars direct return

Case no.	Initial velocity, m/s	Initial flight-path angle, deg	Ballistic coefficient (~Mach 30), kg/m^2
0	14,008	−7.20	356
1	12,201	−5.09	122
2	12,201	−5.61	488
3	12,201	−6.63	122
4	12,201	−7.40	488
5	16,007	−5.93	122
6	16,007	−6.53	488
7	16,007	−6.43	122
8	16,007	−7.08	488
9	14,008	−5.58	122
10	14,008	−5.21	49

cases. Initial conditions for the 18 cases (three velocities, three ballistic coefficients, minimum and maximum flight-path angle) are listed in Table 4.

Operationally, it was assumed that the vehicle would perform a single pass through Earth's atmosphere (as opposed to aerobraking, i.e., multiple passes) to achieve the desired apogee and would then perform a propulsive burn to raise the perigee to a sustainable orbit, if required. At that point two return scenarios were considered: 1) The vehicle could loiter in orbit for some predetermined time until the range is clear or until properly aligned with the landing site and then reenter, or 2) the vehicle could instead rendezvous and dock with a separate system already in orbit. In the case of a manned mission, the crew could transfer into the other system for reentry and return to Earth's surface. In the second scenario the original system would remain in orbit and not reenter. To accommodate the situation in which the "captured" vehicle is also tasked to perform the reentry, three additional trajectory cases were generated for Earth reentry from a 500-km circular orbit (subsequent to a deorbit burn), one each

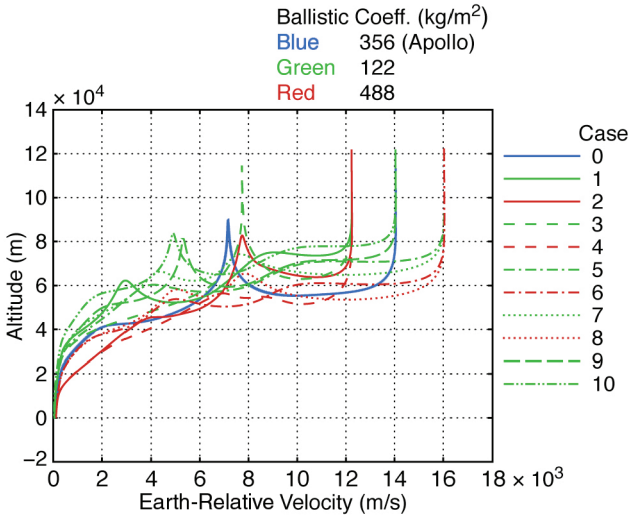

Fig. 12 Geodetic altitude as a function of Earth-relative velocity for all Mars direct Earth return cases.

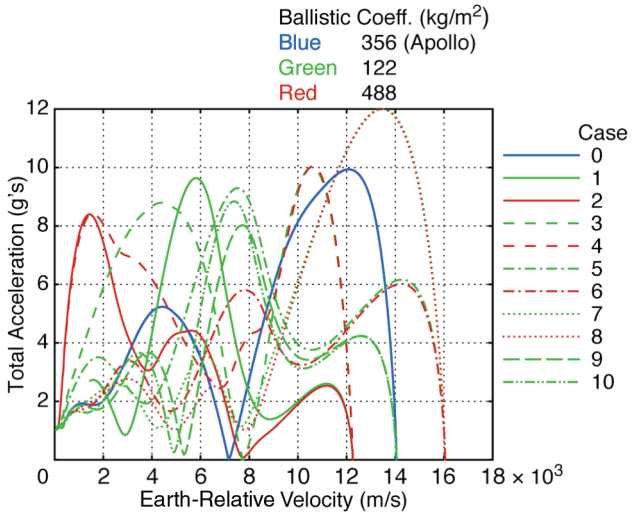

Fig. 13 Total sensed acceleration as a function of Earth-relative velocity for all Mars direct Earth return cases.

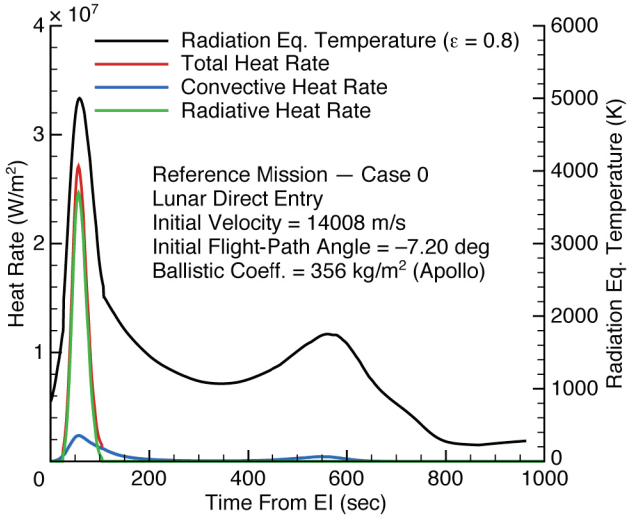

Fig. 14 Stagnation region heating profile for the nominal Mars direct Earth-entry case.

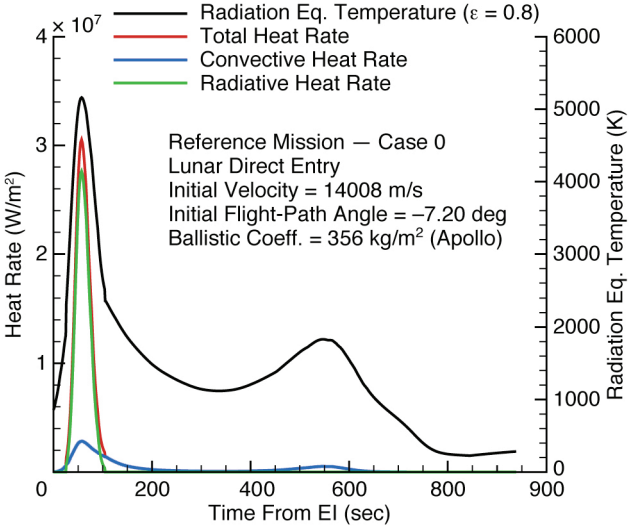

Fig. 15 Hot corner heating profiles for the nominal Mars direct Earth-entry case.

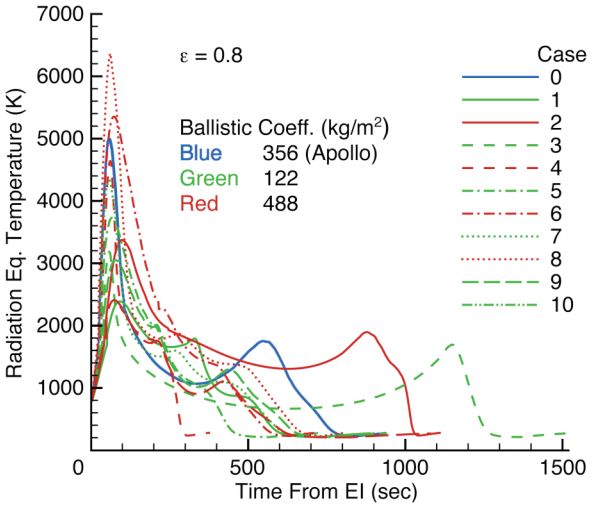

Fig. 16 Stagnation region radiation equilibrium temperature for all Mars direct Earth return cases.

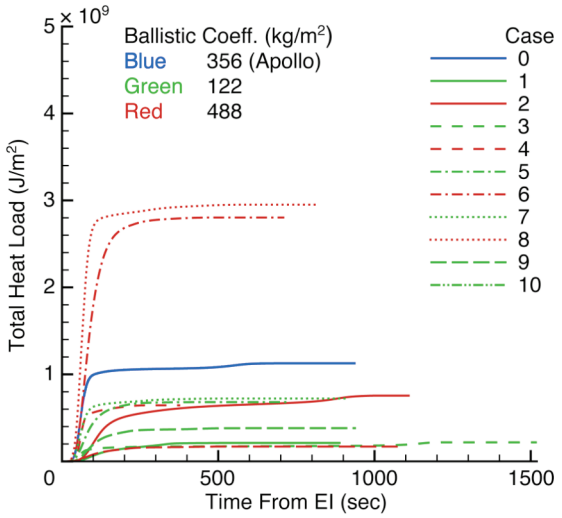

Fig. 17 Stagnation region integrated heat load for all Mars direct Earth return cases.

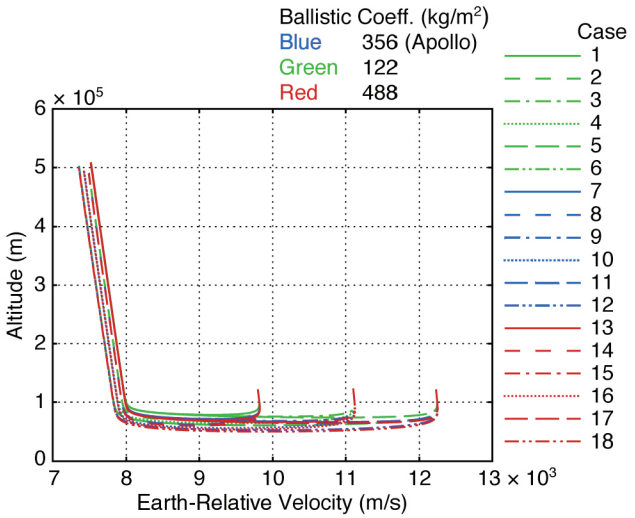

Fig. 18 Geodetic altitude as a function of Earth-relative velocity for Earth aerocapture at lunar return conditions.

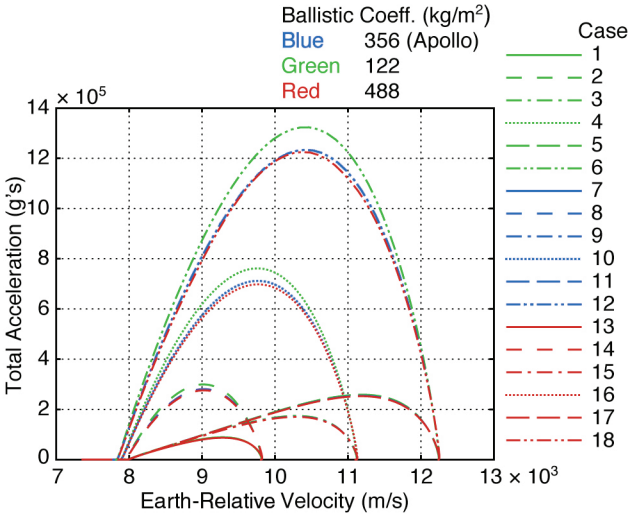

Fig. 19 Total sensed acceleration as a function of Earth-relative velocity for Earth aerocapture at lunar return conditions.

for the high, medium, and low ballistic coefficients. To model the entire aerocapture, entry, and landing sequence, the heating information for the reentry from LEO cases would be appended to the appropriate aerocapture case.

For the aerocapture portions, plots of altitude and acceleration as functions of Earth-relative velocity are shown in Figs. 18 and 19, respectively. Compared to the direct entry cases, these cases are much better behaved, primarily due to the fact that no steering (bank

Table 4 Trade matrix for Earth aerocapture at lunar return conditions

Case no.	Initial velocity, m/s	Initial flight-path angle, deg	Ballistic coefficient (~Mach 30), kg/m^2
1	9,765	−3.78	122
2	9,765	−4.78	122
3	11,075	−4.62	122
4	11,075	−6.28	122
5	12,201	−5.09	122
6	12,201	−7.29	122
7	9,765	−4.09	356
8	9,765	−5.07	356
9	11,075	−4.99	356
10	11,075	−6.60	356
11	12,201	−5.49	356
12	12,201	−7.64	356
13	9,765	−4.19	488
14	9,765	−5.15	488
15	11,075	−5.10	488
16	11,075	−6.70	488
17	12,201	−5.61	488
18	12,201	−7.74	488

angle modulation) was implemented in the aerocapture cases. This lack of steering, however, does contribute to higher accelerations for the higher entry velocities. This is even more evident for the aerocapture from Mars cases discussed in the next section. It should be noted that with steering, there would basically be an infinite number of trajectories for each combination of ballistic coefficient and entry velocity that exists between the minimum and maximum flight-path angles shown in Table 4, and thus peak acceleration loads could be mitigated fairly easily. Figures 20 and 21 show the relative levels of heating at the stagnation and hot corner locations for the nominal case. Again, note that the heating levels for these two regions are similar in nature, though the hot corner experiences about 20% higher heating rates. Figures 22 and 23 show the radiation equilibrium temperature and integrated heat loads for all 18 Earth aerocapture from lunar return cases. Looking at Fig. 22, it is clear that several of the shallow entries could lend themselves to the use of reusable CMCs.

VI. Earth Aerocapture from Mars Return Conditions

The low, medium, and high values of initial velocity and ballistic coefficient used for the Earth aerocapture from Mars return conditions are the same as those selected for direct entry from Mars. Initial conditions for the 18 cases (three velocities, three ballistic coefficients, minimum and maximum flight-path angles) are listed in Table 5.

Plots of altitude and acceleration as functions of Earth-relative velocity are shown in Figs. 24 and 25, respectively. Figures 26 and 27 show heating rate profiles for case 1 for the stagnation region and hot corner, respectively. Note again that the hot corner sees about 15% more heating than the stagnation region. Figure 28 shows stagnation region heating for case 5, which has the same ballistic coefficient as case 1, but is at the higher entry velocity (16 km/s compared to 12.2 km/s for case 1). Notice that for the case 5 stagnation region profile, the peak radiative heating rate is more than 5.5 times higher than the convective. Figures 29 and 30 show the radiation equilibrium temperature and integrated heat loads, respectively, for all 18 Earth aerocapture at Mars return conditions. Note that only case 1, at the lowest velocity and ballistic coefficient, and shallowest flight-path angle, even approaches the temperature limit defined for reusable materials. Thus, all the aerocapture cases at Mars return conditions would require the use of an ablative TPS system.

VII. Reentry from Low-Earth Orbit

As described previously, in some aerocapture scenarios, the vehicle that performs the aerocapture maneuver may also at some point reenter from LEO. For this scenario, three additional

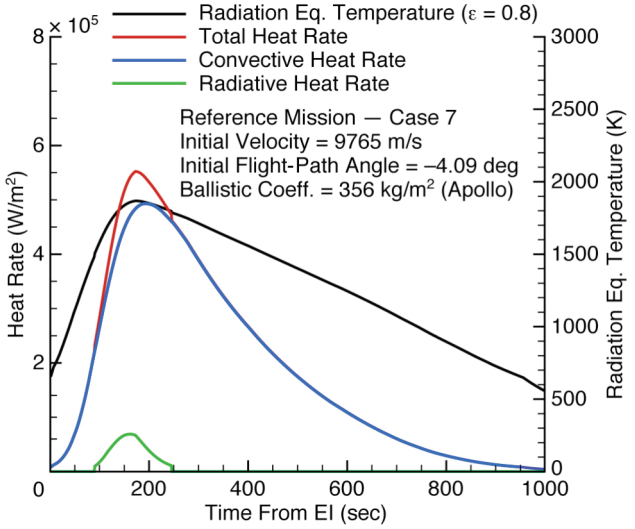

Fig. 20 Stagnation region heating profiles for Earth aerocapture at lunar return conditions, case 7.

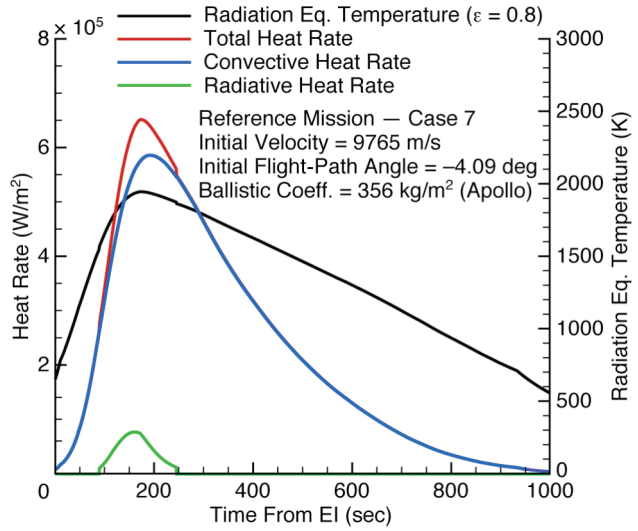

Fig. 21 Hot corner heating profiles for Earth aerocapture at lunar return conditions, case 7.

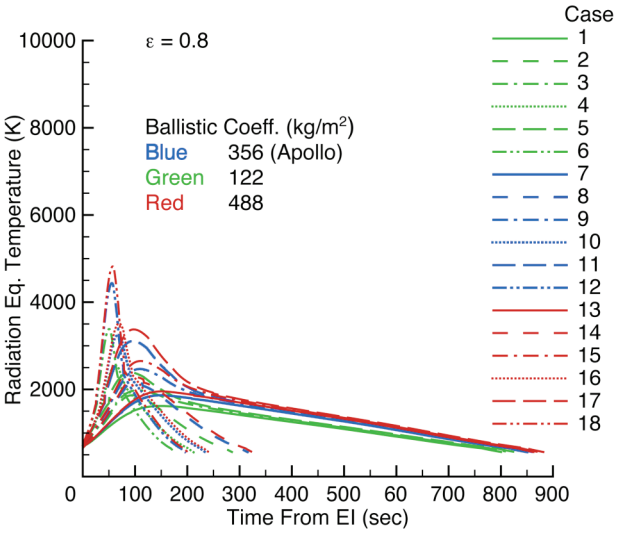

Fig. 22 Stagnation region radiation equilibrium temperatures for all Earth aerocapture cases at lunar return conditions.

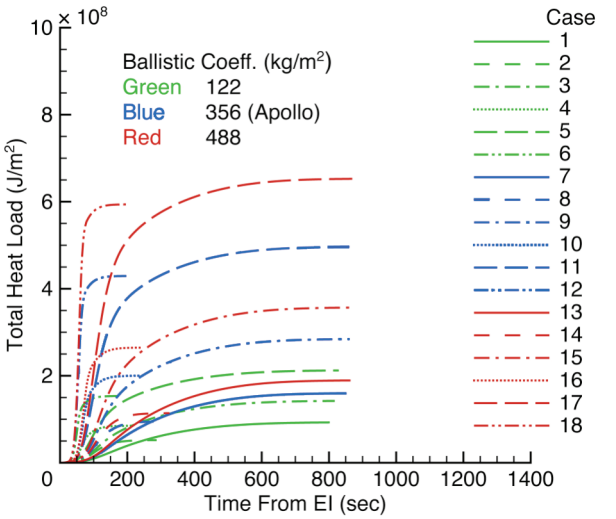

Fig. 23 Stagnation region integrated heat loads for all Earth aerocapture cases at lunar return conditions.

Table 5 Trade matrix for Earth aerocapture at Mars return conditions

Case no.	Initial velocity, m/s	Initial flight-path angle, deg	Ballistic coefficient (~Mach 30), kg/m^2
1	12,201	−5.09	122
2	12,201	−7.29	122
3	14,008	−5.58	122
4	14,008	−8.63	122
5	16,007	−5.93	122
6	16,007	−9.86	122
7	12,201	−5.49	356
8	12,201	−7.64	356
9	14,008	−6.02	356
10	14,008	−8.98	356
11	16,007	−6.39	356
12	16,007	−10.18	356
13	12,201	−5.61	488
14	12,201	−7.74	488
15	14,008	−6.15	488
16	14,008	−9.07	488
17	16,007	−6.53	488
18	16,007	−10.27	488

trajectories were generated for an Earth reentry from a 500-km circular orbit one each for the high, medium, and low ballistic coefficients. To model the entire aerocapture, entry, and landing sequence, the heating information for the reentry from LEO cases should be appended to the appropriate aerocapture case. An initial entry velocity of 7.957 km/s and flight-path angle of −1.6 deg were assumed for all entries from LEO. This entry mode from LEO also satisfies the crew transport mission to and from the International Space Station, which will be required after the retirement of the Space Shuttle Orbiter presently scheduled for 2010.

Figure 31 shows the altitude-velocity profiles for the three LEO entry cases, including a representative shuttle entry, STS-28, for comparison. Figures 32 and 33 highlight the radiation equilibrium temperature and integrated heat loads for the entry from LEO cases. Despite the lower flight performance when compared to the Shuttle Orbiter, the three LEO return cases fall within the temperature capability range assumed for reusable materials, less than 2000 K. Note also that the LEO return heat rates and loads are significantly less than all but the most benign cases for direct or aerocapture return at lunar or Mars entry conditions.

VIII. Summary

Figure 34 summarizes the results of the heating environment trade over the five return mission scenarios and range of ballistic coefficients, entry flight-path angles, and velocities considered. Data are presented in terms of radiation equilibrium temperature to enable assessment based on maximum TPS/material concept temperature limits. A constant emissivity of 0.8, representative of a coated reusable system, is assumed for the radiation equilibrium temperature calculation. For each mission type, the range of peak radiation equilibrium temperature values for either location (hot corner or stagnation region, whichever is greater) over the associated trade space is identified. Cases highlighted in red exceed the 2000 K limit set for reusable materials, and therefore necessitate the use of an ablative system or another high-temperature system. For cases highlighted in green, reusable systems may be feasible. In general, Mars return requires the use of ablative systems while the return from LEO can typically be accomplished using a reusable system.

IX. Conclusions

More than 60 unique entry trajectories and the associated aeroheating environments were generated to assist designers in the development of TPS systems and related testing environments for the Crew Exploration Vehicle. Using the Apollo Command Module as the baseline entry system, trajectories and aerothermal environments for a range of lunar and Mars return, direct and aerocapture Earth-entry scenarios were developed. The range of trajectories and environments that were generated were intended to bound the range of potential entry scenarios, vehicle characteristics, and TPS requirements for likely CEV concepts. Results show that, over the

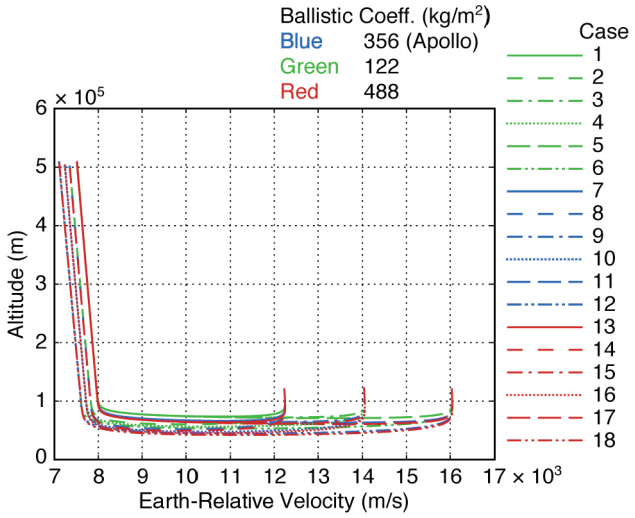

Fig. 24 Geodetic altitude as a function of Earth-relative velocity for all Earth aerocapture cases at Mars return conditions.

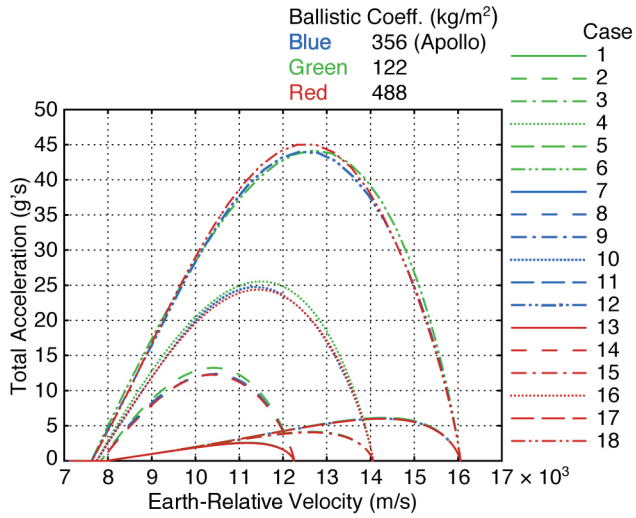

Fig. 25 Total sensed acceleration as a function of Earth-relative velocity for all Earth aerocapture cases at Mars return conditions.

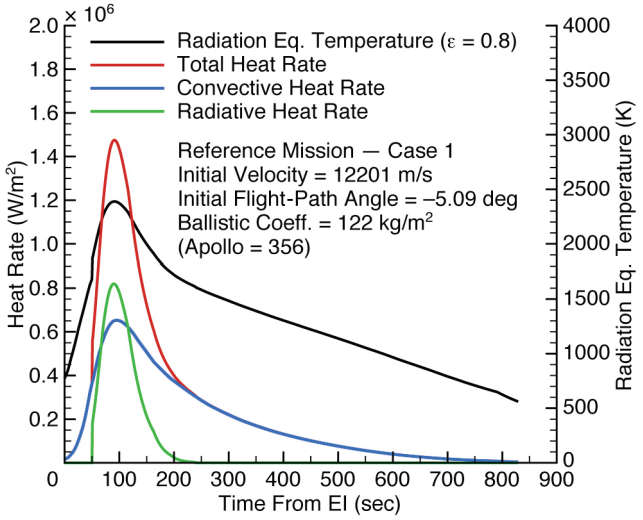

Fig. 26 Stagnation region heating profiles for Earth aerocapture at Mars return conditions, case 1.

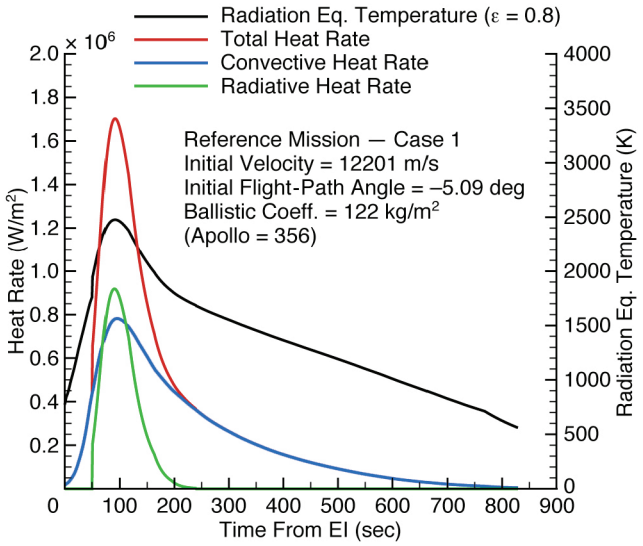

Fig. 27 Hot corner heating profiles for Earth aerocapture at Mars return conditions, case 1.

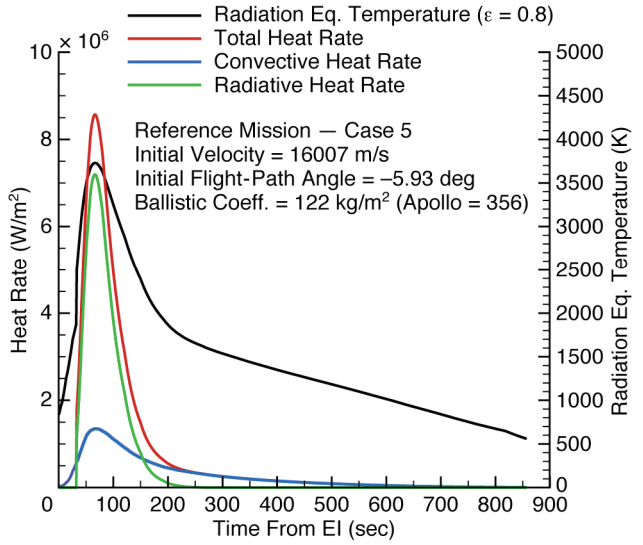

Fig. 28 Stagnation region heating profiles for Earth aerocapture at Mars return conditions, case 5.

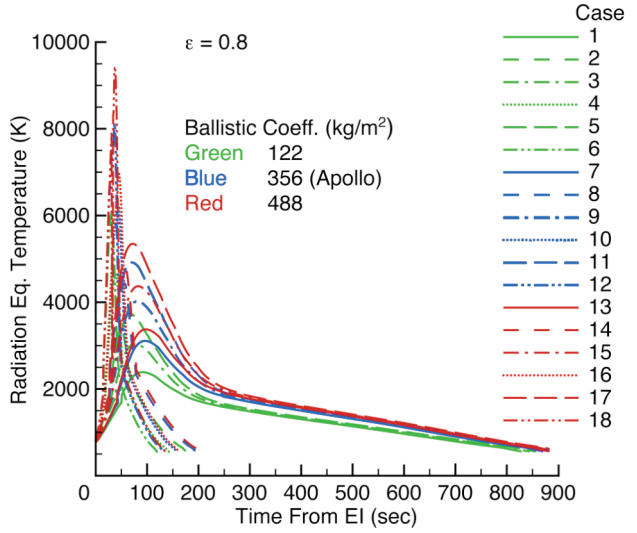

Fig. 29 Stagnation region radiation equilibrium temperatures for all Earth aerocapture cases at Mars return conditions.

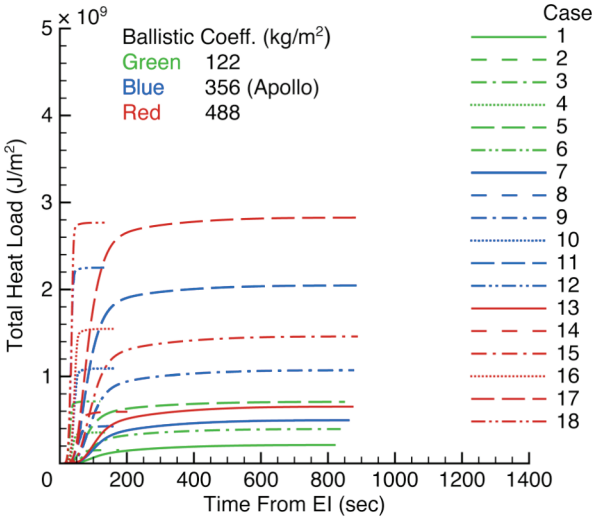

Fig. 30 Stagnation region integrated heat loads for all Earth aerocapture cases at Mars return conditions.

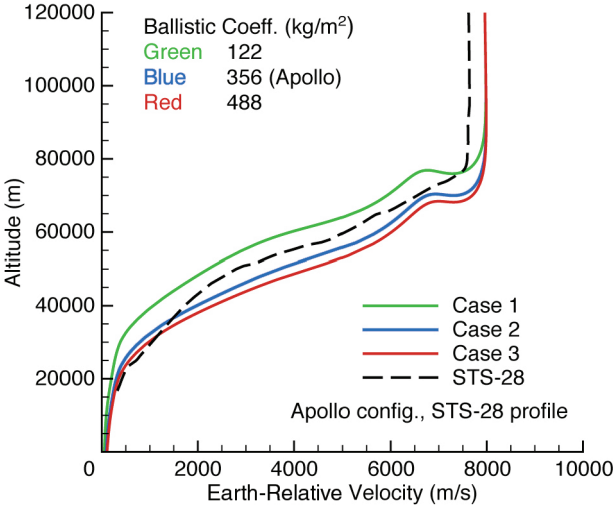

Fig. 31 Geodetic altitude as a function of Earth-relative velocity for reentry from low-Earth orbit.

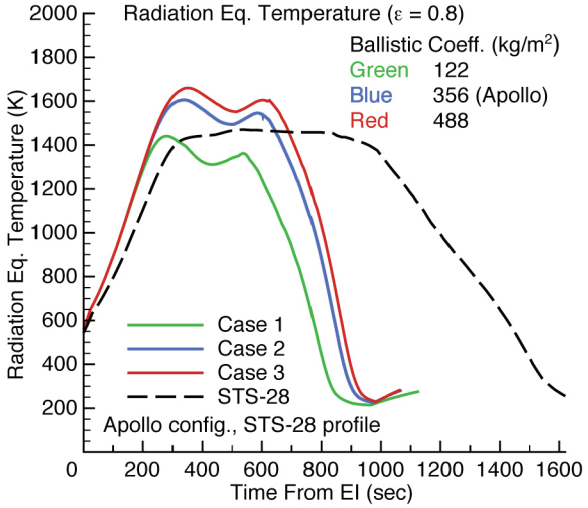

Fig. 32 Stagnation region radiation equilibrium temperatures for reentry from low-Earth orbit cases.

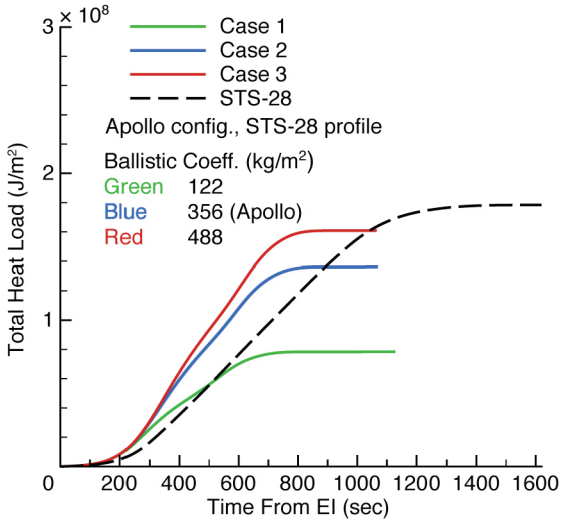

Fig. 33 Stagnation region integrated heat loads for reentry from low-Earth orbit cases.

range of vehicle ballistic coefficients considered, all Mars return missions, both direct and aerocapture, will require the use of ablative systems. Several will likely require additional deceleration devices to slow the vehicle to speeds, and thus heating rates, for which existing ablative TPS may be feasible. LEO return missions can generally be accomplished with reusable material systems. For the lunar return scenarios considered, there exist some combinations of low ballistic coefficients and entry velocities that may be accomplished with ablative systems, but the most likely return conditions will require at least some use of ablative systems. In addition, the results clearly indicate the entry conditions and modes most suitable for manned flight, considering vehicle deceleration levels experienced during entry, although many suitable trajectories exist within the design space explored. Work is currently underway within several NASA projects to improve the modeling capability for radiative heating environments, turbulent/transition heating predictions, coupled radiative/convective environments, as well as coupled flowfield/ablation analyses. As these efforts mature, the TPS material testing capabilities that will be required will become more clearly defined. Until that time, the aeroheating environments generated in this study provide a reasonable first estimate and may be used by the vehicle designer to assess the material testing limits and facility requirements for a broad range of vehicle concepts and missions.

Mission Mode	Peak Temperature* Range			
	Stagnation and Corner Conditions Combined			
	(K)		(°F)	
	Low	High	Low	High
Lunar Direct	1699	4785	2599	8153
Mars Direct	2390	6598	3842	11417
Lunar Aerocapture	1619	4969	2455	8485
Mars Aerocapture	2388	9771	3839	17128
Low Earth Orbit	1440	1736	2132	2665

*Radiation Eq. Temperature based on emissivity of 0.80.

Note: All minimums occur in stagnation area, maximums at corner.

Fig. 34 Peak temperature summary for the stagnation point and hot corner locations for all five mission-mode trade matrices.

References

[1] "The Vision for Space Exploration," National Aeronautics and Space Administration (NASA), Feb. 2004, http://www.fas.org/irp/offdocs/nspd/nspd-31.pdf.

[2] "Apollo Master Spacecraft Specification: Exhibit I, Paragraph 4.2," North American Aviation, Inc., NAS 9-150, 31 Oct. 1963.

[3] Striepe, S. A., Powell, R. W., Desai, P. N., Queen, E. M., Brauer, G. L., Cornick, D. E., Olson, D. W., Petersen, F. M., Stevenson, R., Engel, M. C., Marsh, S. M., and Gromoko, A. M., "Program to Optimize Simulated Trajectories (POST II), Vol. II Utilization Manual," Ver. 1.1.6.G, NASA Langley Research Center, Hampton, VA.

[4] Striepe, S. A., Way, D. W., Dwyer, A. M., and Balaram, J., "Mars Smart Lander Simulations for Entry, Descent, and Landing," *Journal of Spacecraft and Rockets*, Vol. 43, No. 2, 2006, pp. 311–323. doi:10.2514/1.19649

[5] Raiszadeh, B., and Queen, E. M., "Partial Validation of Multibody Program to Optimize Simulated Trajectories II (POST II) Parachute Simulation with Interacting Forces," NASA TM-2002-211634, 2002.

[6] Tartabini, P. V., Braun, R. D., and Chowdhry, R. S., "A Comparison of Direct Trajectory Optimization Techniques; Collocation vs. Numerical Integration," AIAA Paper 1995-3481, 1995.

[7] U.S. Standard Atmosphere, National Oceanic and Atmospheric Administration, NASA and U.S. Air Force, Washington, D.C., Oct. 1976.

[8] Graves, C. A., and Harpold, J. C., "Apollo Experience Report—Mission Planning for Apollo Entry," NASA TN D-6725, March 1972.

[9] Orloff, R. W., "Apollo By the Numbers: A Statistical Reference for the Manned Phase of Project Apollo," NASA SP-2000-4029, revised Sept. 2004.

[10] Anon., Constellation Program Human-Systems Integration Requirements, NASA, CxP 70024 Baseline, 15 Dec. 2006.

[11] Wurster, K. E., Mills, J. C., and Kamhawi, H., "A Simplified Approach for the Rapid Generation of Transient Heat-Shield Environments," AIAA Paper 2007-411, Jan. 2007.

[12] Engel, C. D., and Praharaj, S. C., "MINIVER Upgrade for the AVID System, Vol. I: LANMIN User's Manual," NASA CR-172212, 1983.

[13] Wurster, K. E., and Stone, H. W., "Aerodynamic Heating Environment Definition/Thermal Protection System Selection for the HL-20," *Journal of Spacecraft and Rockets*, Vol. 30, No. 5, 1993, pp. 549–557. doi:10.2514/3.25565

[14] Wurster, K. E., Riley, C. J., and Zoby, E. V., "Engineering Aerothermal Analysis for X-34 Thermal Protection System Design," *Journal of Spacecraft and Rockets*, Vol. 36, No. 2, 1999, pp. 216–228. doi:10.2514/2.3452

[15] Tartabini, P. V., Wurster, K. E., Korte, J. J., and Lepsch, R. A., "Multidisciplinary Analysis of a Lifting Body Launch Vehicle," *Journal of Spacecraft and Rockets*, Vol. 39, No. 5, 2002, pp. 788–795. doi:10.2514/2.3880

[16] Wurster, K. E., Zoby, E. V., and Thompson, R. A., "Flowfield and Vehicle Parameter Influence on Results of Engineering Aerothermal Methods," *Journal of Spacecraft and Rockets*, Vol. 28, No. 1, 1991, pp. 16–22. doi:10.2514/3.26203

[17] Zoby, E. V., Thompson, R. A., and Wurster, K. E., "Aeroheating Design Issues for Reusable Launch Vehicles—A Perspective," AIAA Paper 2004-2535, June 2004.

[18] Fay, J. A., and Riddell, F. R., "Theory of Stagnation-Point Heat Transfer in Dissociated Air," *Journal of Aeronautical Sciences*, Vol. 25, No. 2, 1958, pp. 73–85,121.

[19] Tauber, M. E., and Sutton, K., "Stagnation-Point Radiative Heating Relations for Earth and Mars Entries," *Journal of Spacecraft and Rockets*, Vol. 28, No. 1, 1991, pp. 40–42. doi:10.2514/3.26206

[20] Sutton, K., and Hartung, L. C., "Equilibrium Radiative Heating Tables for Earth Entry," NASA TM-102652, May 1990.

[21] Sutton, K., "Air Radiation Revisited," *Thermal Design of Aeroassisted Orbital Transfer Vehicles*, edited by H. F. Nelson, Vol. 96, Progress in Astronautics and Aeronautics, AIAA, New York, 1985, pp. 419–441.

[22] Zoby, E. V., and Sullivan, E. M., "Effects of Corner Radius on Stagnation-Point Velocity Gradients on Blunt Axisymmetric Bodies," NASA TM X-1067, March 1965.

[23] Ried, R. C., Jr., Rochelle, W. C., and Milhoan, J. D., "Radiative Heating to the Apollo Command Module: Engineering Prediction and Flight Measurement," NASA TM X-58091, April 1972.

[24] Hoshizaki, H., "Heat Transfer in Planetary Atmospheres at Super-Satellite Speeds," *ARS Journal*, Vol. 32, No. 10, Oct. 1962, pp. 1544–1552.

[25] Sutton, K., and Graves, R. A., Jr., "A General Stagnation-Point Convective-Heating Equation for Arbitrary Gas Mixtures," NASA TR R-376, Nov. 1971.

[26] Johnston, C. O., "A Comparison of EAST Shock-Tube Radiation Measurements with a New Air Radiation Model," AIAA Paper 2008-1245, Jan. 2008.

[27] Bose, D., McCorkle, E., Thompson, C., Bogdanoff, D., Prabhu, D. K., Allen, G. A., and Grinstead, J., "Analysis and Model Validation of Shock Layer Radiation in Air," AIAA Paper 2008-1246, Jan. 2008.

[28] Thompson, R. A., and Gnoffo, P. A., "Implementation of a Blowing Boundary Condition in the LAURA Code," AIAA Paper 2008-1242, Jan. 2008.

T. Lin
Associate Editor